RESEARCH ARTICLE | APRIL 25 2023

Amplification of turbulent kinetic energy and temperature fluctuation in a hypersonic turbulent boundary layer over a compression ramp ⊘

Special Collection: Hypersonic Flow

Guo Tongbiao (郭同彪) ⓘ ; Zhang Ji (张吉) ⓘ ; Tong Fulin (童福林) ⓘ ; Li Xinliang (李新亮) ✉ ⓘ

Check for updates

View Online   Export Citation

Physics of Fluids

Special Topic:
Flow and Civil Structures

Submit Today

AIP Publishing

Amplification of turbulent kinetic energy and temperature fluctuation in a hypersonic turbulent boundary layer over a compression ramp

Tongbiao Guo (郭同彪),[1] [iD] Ji Zhang (张吉),[1,2] [iD] Fulin Tong (童福林),[3] [iD] and Xinliang Li (李新亮)[1,2,a] [iD]

AFFILIATIONS

[1]LHD, Institute of Mechanics, Chinese Academy of Sciences, Beijing 100190, China
[2]School of Engineering Science, University of Chinese Academy of Sciences, Beijing 100049, China
[3]State Key Laboratory of Aerodynamics, 621000 Mianyang, China

Note: This paper is part of the special topic, Hypersonic Flow.
[a]Author to whom correspondence should be addressed: lixl@imech.ac.cn

ABSTRACT

In this paper, direct numerical simulations in a Mach 6.0 hypersonic turbulent boundary layer over a 30° compression ramp are performed. The influence of shock wave/boundary layer interactions on the amplification of turbulent kinetic energy (TKE) and temperature fluctuation (TF) is explored, to provide an insight into the physical mechanism. In the initial part of the interaction region before the detachment of the shear layer, the amplification of the TKE and TF is found, via a frequency spectrum analysis, to be closely related to the low-frequency unsteadiness of the shock wave. Once the free shear layer is established, the shear component of the TKE production defined in the shear layer coordinate appears to act as the main contributor for the TKE amplification, owing to the mixing layer turbulence and the resultant Kelvin–Helmholtz instability. This is consistent with the result from the spectrum analysis that the TKE and TF amplification and their streamwise evolution are dominated by the spectral energy in the median-frequency range, arising from the mixing layer turbulence. As the flow moves downstream along the shock wave, the high-frequency spectral energy content of TF shows a decreasing trend, while the low-frequency spectral energy tends to increase gradually, implying that the shock wave low-frequency unsteadiness exists not only in the initial stage of the interaction region but also around the main shock wave. Under the combined influence of the shock wave intensity and interaction intensity, the median-frequency content appears to weaken first and then tends to increase before decreasing again. The variation amplitude appears to be small and generally dominates the distribution of the TF intensity.

Published under an exclusive license by AIP Publishing. https://doi.org/10.1063/5.0145320

I. INTRODUCTION

Shock wave/turbulent boundary layer interactions (SWTBLIs) occur widely in supersonic/hypersonic flows relevant to aircraft, missiles, and rockets. They can induce complex flow phenomena[1] (shock wave unsteadiness, flow separation, turbulence amplification, etc.) and consequently cause significant pressure fluctuations and heat loads in engineering applications, which may lead to increased flight drag and structural failure. In consequence, it is of importance, in order to alleviate these detrimental effects, to achieve comprehensive understanding of SWTBLIs.

Among the complex flow phenomena in SWTBLIs, the amplification of turbulence has received great research attention in the past decades.[2–5] Smits and Muck[2] conducted experimental investigation to study the supersonic turbulent boundary layer over 8°, 16°, and 20° compression ramps. They found that the SWTBLIs amplified the turbulent fluctuations significantly, and the amplification appeared to increase with increasing turning angles. They also pointed out that when the shock wave intensity was relatively low, the turbulence amplification was mainly caused by the pressure rise, compressive extra strain rates, and concave curvature. As the shock wave intensity increased, the oscillation of the shock wave tended to pump energy from the mean flow into turbulent fluctuations and played the dominant role on the amplification. Selig *et al.*[6] performed experiments in the supersonic wind tunnel to study the SWTBLIs over a 24° compression ramp. Their results indicated that the turbulence amplification in the upstream part of the interaction region was caused by the

unsteady shock wave motion, while for the downstream part, the amplification might arise from unsteady streamwise Taylor–Görtler type vortices. Wu and Martín[7] carried out direct numerical simulation (DNS) of a turbulent boundary layer over a 24° compression ramp at Mach 2.9. Their simulation results showed that the Reynolds stresses were greatly amplified, and the amplification factors were up to 6–24. They suggested that, as reported by Selig et al.,[6] the unsteady shock wave motion and concave streamline curvature were responsible for the turbulence amplification. The similar results were observed in the DNS of impinging SWTBLIs by Priebe et al.[8] with the incident shock wave of 12°. Pirozzoli and Grasso[9] conducted DNS of supersonic impinging shock wave/boundary layer interaction flows. Their results revealed that the turbulent kinetic energy (TKE) was amplified through the interaction region, and the maximum value was about 2.7 times its peak value in the upstream undisturbed turbulent boundary layer. They attributed the amplification mechanism to the formation of the mixing layer. Dupont et al.[3] experimentally studied SWTBLIs at Mach 2.3 using particle image velocimetry. They found that the streamwise evolution of the maximum TKE followed the core of the separated shear layer, and this phenomenon supported the finding of Pirozzoli and Grasso.[9] The similar flow phenomena were also observed in the DNS study of SWTBLIs over a 24° compression ramp by Priebe and Martín,[10] who reported that the turbulence amplification could be attributed to the energetic turbulent structures generated in the mixing layer and the shedding of these turbulent structures into the downstream flow. According to Dupont et al.[11] and Helm et al.,[12] the separated shear layer was essentially a compressible mixing layer, following the properties of the canonical mixing layer. In their work, large-scale mixing-layer-like vortical rollers were observed in the separated shear layer, inferring that the amplification of turbulence might be dominated by the formation of the mixing layer and the Kelvin–Helmholtz instability. Fang et al.[5] conducted DNS of impinging SWTBLIs at Mach 2.25 and proposed a new turbulence amplification mechanism. They found that in the initial stage of the interaction, the turbulence amplification was due to the deceleration of the mean flow along with the increased streamwise velocity fluctuations, while in the downstream part, the amplification was mainly caused by the free shear layer. Yu et al.[13] studied the turbulence amplification in a supersonic impinging shock wave/boundary layer interaction flow from the view of spanwise energy spectra. They reported that as the flow entered the interaction region, the most energetic motions were converted from the near-wall small-scale motions to large-scale motions, and the streamwise velocity fluctuation amplification was triggered first, resulting in the emergence of large-scale velocity streaks.

Another noteworthy important feature of turbulent amplification is the temperature fluctuation (TF). According to Morkovin's hypothesis,[14] TF increases as the square of Mach number. Duan et al.[15] conducted DNS of a hypersonic turbulent boundary layer, and it was reported that the strong Reynolds analogy relationship between the TF and the streamwise velocity fluctuation was dependent on the wall temperature. Gerolymos and Vallet[16] investigated the TF in compressible turbulent channel flow. By analyzing the transport equation of TF, they found that dilatational terms were quite weak and negligible. McManamen et al.[17] studied the TF amplification in a supersonic shock wave turbulence interaction. The results showed that the amplification factor varied between 3.0 and 4.5, and the lowest Reynolds

number condition leads to the largest free-stream disturbances and amplification. To date, the study with regard to the TF in SWTBLIs is quite limited and its amplification mechanism in the interaction region needs to be further studied.

In this paper, the DNS in a hypersonic SWTBLI over a 30° compression ramp at Mach 6.0 is conducted. The objectives of this present study are threefold: (1) to analyze the physical mechanism of the TKE and TF amplification across the whole interaction region in hypersonic flow; (2) to provide an insight with regard to the TF amplification around the shock wave; and (3) to explore the influence of the low-frequency unsteadiness, which has attracted extensive research attention,[10,18,19] on the TKE and TF amplification. This paper is organized as follows: In Sec. II, the numerical schemes, computational domain, and numerical validation are described. Section III presents the results and discussions, including the basic flow phenomena in the SWTBLIs, the TKE, and TF as well as the frequency spectrum analysis to explore the amplification mechanism. The influence of the low-frequency unsteadiness on the TKE and TF amplification is also analyzed in Sec. III. Conclusions are finally drawn in Sec. IV.

II. METHODOLOGY
A. Governing equations and numerical schemes

The unsteady, three-dimensional, compressible Navier–Stokes equations in a conservative form can be written in a curvilinear coordinate system (ξ_1, ξ_2, ξ_3) in the following equation:

$$\frac{\partial Q}{\partial t} + \frac{\partial (F_1 - G_1)}{\partial \xi_1} + \frac{\partial (F_2 - G_2)}{\partial \xi_2} + \frac{\partial (F_3 - G_3)}{\partial \xi_3} = 0, \quad (1)$$

where t is the time coordinate; Q represents the conservative variables; F_i and G_i $(i = 1, 2, 3)$ are the convective flux and diffusion terms in the ξ_i direction; they are expressed as

$$Q = J^{-1}\begin{bmatrix} \rho \\ \rho u_1 \\ \rho u_2 \\ \rho u_3 \\ \rho E \end{bmatrix}, \quad F_i = J^{-1}\begin{bmatrix} \rho\left(u_j \dfrac{\partial \xi_i}{\partial x_j}\right) \\ \rho u_1\left(u_j \dfrac{\partial \xi_i}{\partial x_j}\right) + \dfrac{\partial \xi_i}{\partial x_1}p \\ \rho u_2\left(u_j \dfrac{\partial \xi_i}{\partial x_j}\right) + \dfrac{\partial \xi_i}{\partial x_2}p \\ \rho u_3\left(u_j \dfrac{\partial \xi_i}{\partial x_j}\right) + \dfrac{\partial \xi_i}{\partial x_3}p \\ (\rho E + p)\left(u_j \dfrac{\partial \xi_i}{\partial x_j}\right) \end{bmatrix},$$

$$(2)$$

$$G_i = J^{-1}\begin{bmatrix} 0 \\ \dfrac{\partial \xi_i}{\partial x_j}\sigma_{j1} \\ \dfrac{\partial \xi_i}{\partial x_j}\sigma_{j2} \\ \dfrac{\partial \xi_i}{\partial x_j}\sigma_{j3} \\ \dfrac{\partial \xi_i}{\partial x_j}(u_k\sigma_{kj} - q_j) \end{bmatrix},$$

where the standard Einstein notation is adopted with summation on repeated indices with i, j, $k = 1$, 2, and 3; $J = |\frac{\partial(\xi_1, \xi_2, \xi_3)}{\partial(x_1, x_2, x_3)}|$ is the Jacobian of the coordinate transformation matrix; $x_i = (x_1, x_2, x_3)$ represents the streamwise (x), wall-normal (y), and spanwise (z) coordinates, and the corresponding velocity components are u, v, and w, or u_1, u_2, and u_3, respectively; ρ and p are the fluid density and pressure; ρE presents the total energy per unit volume; and $\rho E = \frac{1}{2}\rho u_i u_i + \frac{p}{\gamma-1}$, where γ is the ratio of specific heat and $\gamma = 1.4$; the stress tensor, σ_{ij}, is expressed as

$$\sigma_{ij} = \mu\left(\frac{\partial u_i}{\partial x_j} + \frac{\partial u_j}{\partial x_i} - \frac{2}{3}\frac{\partial u_k}{\partial x_k}\delta_{ij}\right), \qquad (3)$$

where μ is the dynamic viscosity of the fluid and is calculated via the Sutherland's law: $\mu = \mu_0(\frac{T}{T_0})^{1.5}\left(\frac{T_0+110.4}{T+110.4}\right)$ with the reference temperature $T_0 = 110$ K and the viscosity μ_0 at the reference temperature.

The heat flux, q_i, is expressed as

$$q_j = -\kappa\frac{\partial T}{\partial x_j}, \qquad (4)$$

where the thermal conductivity, κ, is given by $\kappa = \mu C_p/Pr$, in which Pr is the Prandtl number with $Pr = 0.7$, and $C_p = \gamma R/(\gamma - 1)$ is the specific heat capacity of the gas at constant pressure with the perfect gas constant $R = 287.1$ J/(kg K).

In the present DNS, an in-house high-order finite difference code (OpenCFD-SC)[20,21] is applied, and it has been used successfully in many supersonic/hypersonic shock wave/turbulent boundary-layer interaction studies.[18,20,22] The convective terms are discretized by a hybrid difference scheme, which adapts its form according to the shock sensor introduced by Jameson et al.[23] The seventh-order upwind discretization is applied in smooth parts of the flow field to maximize the resolving accuracy, while around the shock wave, a seventh/fifth-order WENO (weighted essentially non-oscillatory) scheme is used to preserve the robustness. The diffusion terms are discretized with an eighth-order central difference scheme. After all the spatial terms are solved, a scheme of explicit third-order total-variation-diminishing Runge–Kutta method is applied for the temporal integration.

In this paper, the Reynolds and density-weighted averaging for a general variable ϕ is expressed as $\bar{\phi}$ and $\langle\phi\rangle$, respectively. In consequence, the fluctuations arising from the Reynolds and density-weighted averaging are expressed as $\phi' = \phi - \bar{\phi}$ and $\phi'' = \phi - \langle\phi\rangle$.

B. Computational domain and set-up

The present study is undertaken in a hypersonic turbulent boundary layer over a 30° compression ramp, as seen in Fig. 1. The coordinate system adopted in the present study is shown with its origin located in the compression corner. The streamwise length and height of the computational domain are $L = 82\delta$ and $H = 6.0\delta$, where $\delta = 9.2$ mm is the flat-plate turbulent boundary layer thickness at $x = -8.5\delta$ and is used as the reference length. The spanwise width W is 2.6δ or 5.2δ depending on the cases and will be described later.

The free-stream Mach number Ma_∞ is 6.0, and the free-stream temperature T_∞ is 110.0 K. The Reynolds number based on the momentum thickness θ ($\theta/\delta = 0.036$) of the turbulent boundary layer at $x/\delta = -8.5$ is $Re_\theta = 6620$. The corresponding friction Reynolds
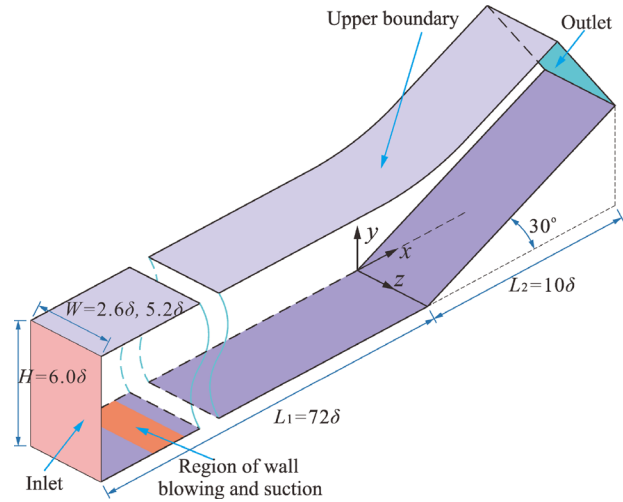

FIG. 1. Sketch of the computational domain and its size in the streamwise, wall-normal, and spanwise directions. δ is the flat-plate turbulent boundary layer thickness at $x = -8.5\delta$.

number $Re_\tau = U_\tau\delta/\bar{\nu}_w$ (U_τ is the mean friction velocity and $\bar{\nu}_w$ is the mean fluid kinematic viscosity at the wall) is 480. The non-dimensional time step Δt is $0.0008\delta/U_\infty$ (U_∞ is the free-stream velocity). After the flow reaches the statistically steady state, the instantaneous flow field is sampled every 5 time steps, and 250 000 samples of instantaneous flow field are collected, covering 1000 δ/U_∞ time range.

The computational domain is bounded by the inlet, outlet, a bottom wall boundary, an upper far-field boundary, and two periodic boundaries in the spanwise direction. At the inlet plane, a steady laminar compressible boundary layer profile is imposed, obtained from the auxiliary simulation of a laminar flat-plate boundary layer using the same free-stream conditions and wall temperature. To induce laminar-to-turbulent transition, wall blowing and suction perturbations[24] ranging from $x/\delta = -70.5$ to $x/\delta = -67.5$ (see Fig. 1) are introduced. To eliminate the disturbance reflection generated through the numerical treatment of the outflow boundary conditions, the grid is progressively coarsened near the outlet and top boundary (see Fig. 2), and the nonreflecting boundary condition is enforced, which allows acoustic, entropy, and vortical waves to propagate out of the computational domain.[25] On the bottom wall, the no-slip boundary condition is enforced together with the wall pressure assumption $\partial\bar{p}/\partial\xi_2 = 0$, and the wall temperature is set to be a constant, $T_w/T_\infty = 5.6$. The periodic boundary condition is used in the spanwise direction.

Three DNS cases are performed in this study, i.e., Case30, Case30B, and Case30C, as depicted in Table I. Case30B and Case30C are conducted for the grid- and domain-sensitivity study. A structured mesh is adopted to discretize the computational domain, and the number of grid nodes in each direction is shown in Table I. The mesh distribution for Case30 in the x–y plane is shown in Fig. 2, where the grid nodes are plotted every 30th nodes in the x and y directions for the sake of visualization. The streamwise resolution of the mesh is also shown in each section of the domain, where the superscript "+" denotes variables in the inner scale, calculated based on the wall units at $x/\delta = -8.5$. In the wall-normal direction, a non-uniform mesh
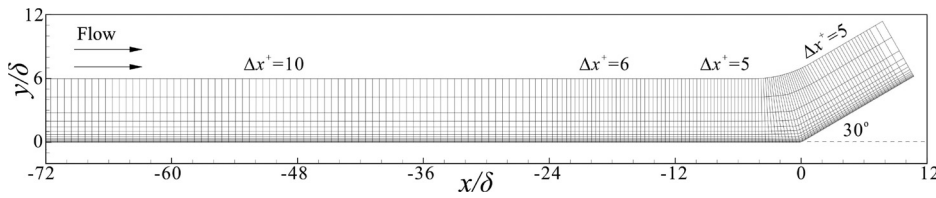
FIG. 2. Mesh distribution in the x–y plane for Case30, where the mesh is plotted every 30th grid line in the x and y directions for the convenience of visualization.

TABLE I. Properties of the incoming flow and mesh distributions for DNS cases. Δx^+ reveals the streamwise grid size of the three streamwise sections in Fig. 2.

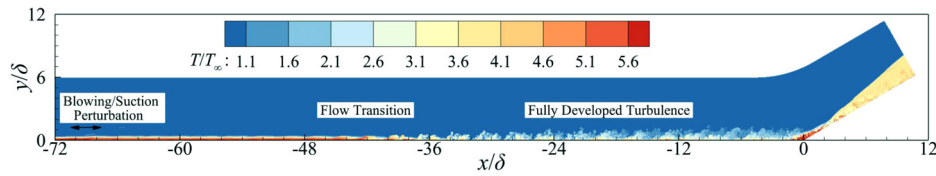| Case	Re_θ	Ma_∞	T_w/T_∞	W/δ	N_x	N_y	N_z	Δx^+	Δy^+	Δz^+
Case30	6620	6.0	5.6	2.6	5300	380	300	10/6/5	0.5 $\sim$	4.0
Case30B	6620	6.0	5.6	2.6	6100	440	430	10/6/3.5	0.35 $\sim$	2.8
Case30C	6620	6.0	5.6	5.2	5300	380	450	10/6/5	0.5 $\sim$	4.0

FIG. 3. Contours of the instantaneous temperature field in a x–y section in the baseline case.

based on a geometric progression with a constant ratio was applied, while in the spanwise direction, the mesh is uniformly distributed.

C. Validation of the numerical method

Figure 3 presents a representative instantaneous temperature field in a x–y section for Case30, to display the entire flow field characteristics. Key features have been observed clearly, including the upstream laminar boundary layer, flow transition, fully developed turbulence, and the shock wave caused by the compression ramp.

In order to verify whether the boundary layer upstream of the shock wave is in a canonical turbulent boundary layer state, Fig. 4(a)

presents the profile of the mean van Driest transformed streamwise velocity. It can be seen that the mean velocity profile obtained from the present simulation at the reference station $x/\delta = -8.5$ agrees well with the classic log-law in the logarithmic region of $30 < y^+ < 100$, verifying that the flow in this region has been fully developed turbulent flow. It is also noteworthy that the constant C in the log-law is around 5.9, larger than that in the incompressible flow (C = 5.1). This finding is consistent with the data from the existed DNS by Zhang et al.,[26] where the free-stream Mach number is the same with the present study at a similar wall-to-recovery temperature ratio.

The profiles of the mean van Driest transformed Reynolds stress at $x/\delta = -8.5$ are plotted in Fig. 4(b). In general, the present results
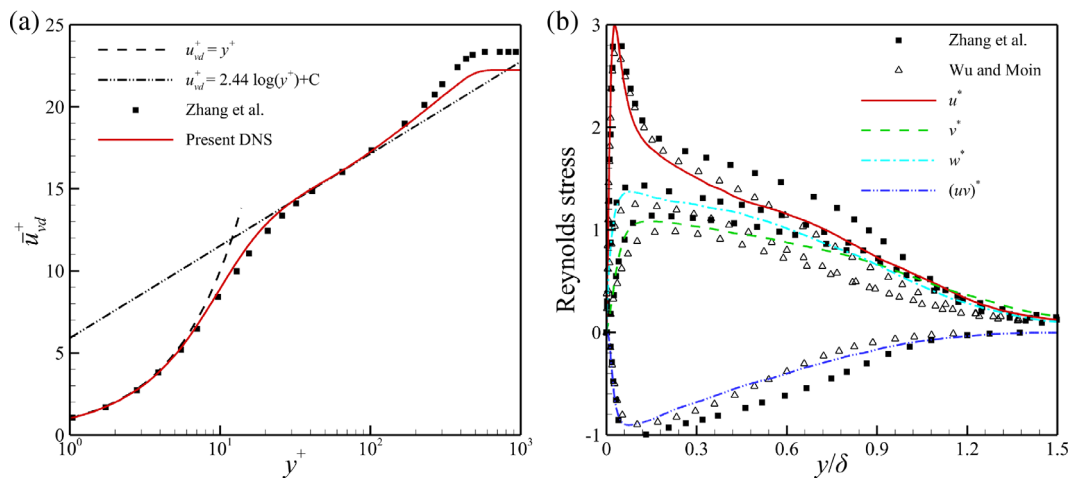

FIG. 4. Profiles of (a) the mean van Driest transformed streamwise velocity and (b) the density-scaled Reynolds stress profiles. The results are extracted at $x/\delta = -8.5$. $y^+ = yU_\tau/\bar{\nu}_w$; $\bar{u}_{vd}^+ = \frac{1}{U_\tau} \int_0^{\bar{u}} \sqrt{\bar{\rho}/\bar{\rho}_w} d\bar{u}$ ($\bar{\rho}_w$ is the mean fluid density at the wall); $u^* = \frac{1}{U_\tau}\sqrt{\bar{\rho}\langle u''u''\rangle/\bar{\rho}_w}$, $(uv)^* = \frac{\bar{\rho}\langle u''v''\rangle}{\bar{\rho}_w U_\tau^2}$.
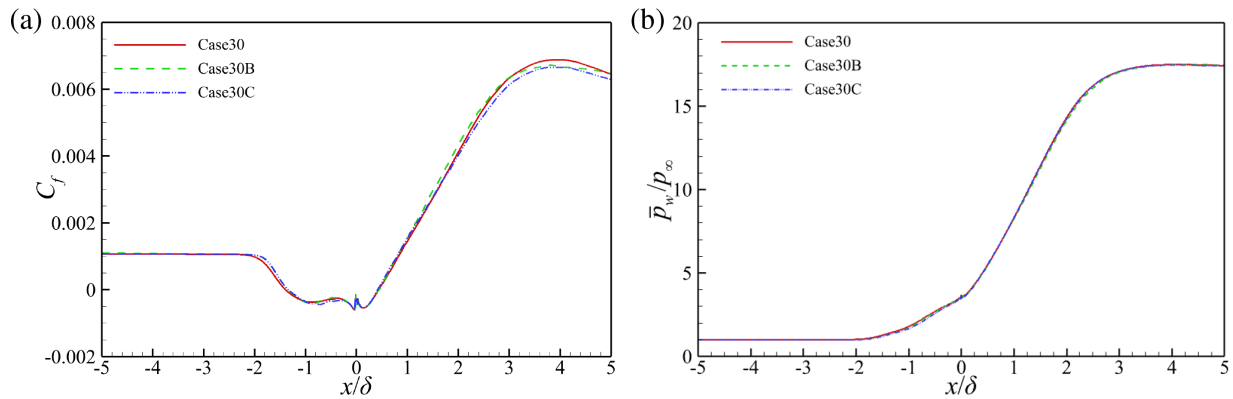
FIG. 5. Streamwise distribution of the mean (a) skin friction coefficient C_f and (b) wall pressure $\bar{p}_w$ around the compression corner.

agree well with the data from Zhang *et al.*[26] and Wu and Moin,[27] indicating that the present DNS in the undisturbed hypersonic turbulent boundary layer is credible.

To ensure that the mesh resolution and the spanwise domain extent are sufficient for the field analysis, a grid- and domain-sensitivity study is performed. In comparison with Case30, the grid number of Case30B doubles with the same domain size; the spanwise width of Case30C doubles with the same grid resolution, as presented in Table I. Figure 5 exhibits the streamwise distribution of the mean skin friction coefficient $C_f = 2\bar{\tau}_w/(\rho_\infty U_\infty^2)$ ($\bar{\tau}_w$ denotes the mean wall shear stress and ρ_∞ is the free-stream fluid density), and the mean wall pressure $\bar{p}_w$ in the vicinity of the compression ramp. Among the three cases, no distinguishable differences can be seen apart from the peak of C_f, where a relative error of less than 3% is observed. In general, the results indicate that the grid resolution and domain size of Case30 are sufficient to perform the following field analysis.

Figure 6 compares the profiles of the turbulent kinetic energy $\langle k \rangle$ at several streamwise positions among the three cases. One can see that the results for the cases are very close to each other with the
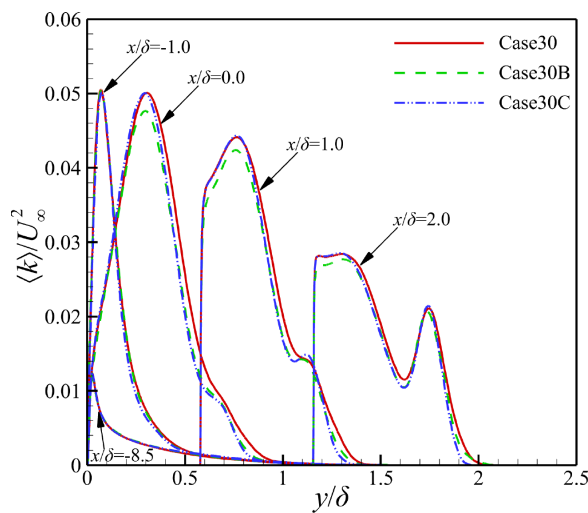
maximum error of about 4.5% near the peak location in the interaction region, which again indicates that the grid resolution and domain size of Case30 are sufficient.

III. RESULTS AND DISCUSSION

In this section, the flow field in the interaction zone is first examined, followed by the analysis of the turbulent kinetic energy and temperature fluctuation.

A. Mean flow characteristics

Figure 7(a) presents contours of the spanwise-averaged mean streamwise velocity in the x–y plane around the compression ramp. The blue line is the isoline of $|\nabla \bar{p}|\delta/\bar{p}_\infty = 10$ denoting the shock

FIG. 6. Profiles of the turbulent kinetic energy $\langle k \rangle$ at several streamwise positions.
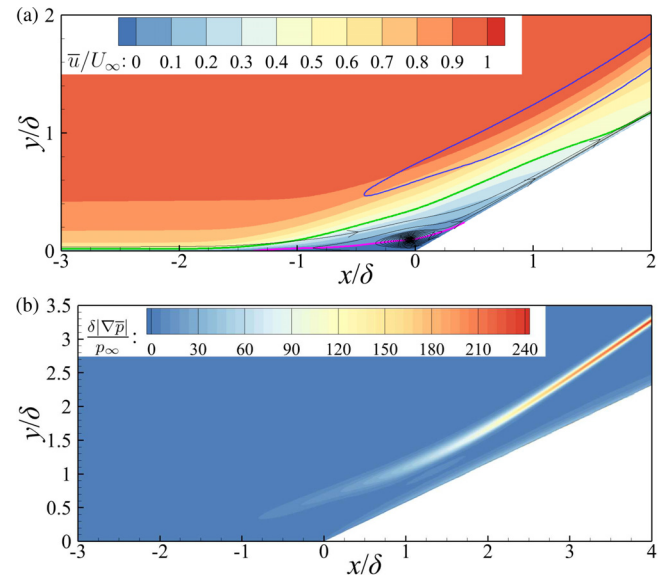

FIG. 7. Contours of the spanwise-averaged (a) mean streamwise velocity superimposed with the streamlines and (b) the mean pressure gradient in the x–y plane. The pink line depicts the locus of zero-streamwise-velocity. The green and blue lines denote the isoline of $\overline{M_a} = 1.0$ and $|\nabla \bar{p}|\delta/\bar{p}_\infty = 10$.

wave, and the contour of $|\nabla \bar{p}| \delta / \bar{p}_\infty$ is also shown in Fig. 7(b). As the flow approaches the compression ramp, the streamwise velocity in the near-wall region tends to decrease significantly, caused by the negative pressure gradient. The green line in Fig. 7(a) denotes the isoline of the mean Mach number $\overline{M_a} = 1.0$. It is clear that the compression ramp leads to significantly enlarged region with low $\overline{M_a}$, and the sonic line tends to move away from the wall, leading to a large subsonic region.

The pink line in Fig. 7(a) depicts the locus of the zero-streamwise-velocity with its starting and ending points denoting the location of the flow separation and reattachment, respectively, and the mean flow separation occurs in the region below the pink line. From Fig. 5(a), one can see that once entering the interaction zone, the wall skin friction appears to drop sharply. The flow separation and reattachment points are located at $x/\delta = -1.4$ and $x/\delta = 0.4$, respectively. The length of the separation zone is defined as the streamwise length between the separation and reattachment points, which is 1.8δ. According to Fig. 5(b), the wall pressure $\bar{p}_w$ across the interaction region appears to increase monotonically. Around the compression corner, there exists a pressure plateau, a typical flow phenomenon for SWTBLI flows with mean flow separation.

B. Unsteadiness of the shock wave

To illustrate the shock wave unsteadiness in the interaction region, contour of the weighted power spectrum of the wall pressure $[WPSD = f * PSD(f) / \int PSD(f) df$, where PSD is the power spectral density], is shown in Fig. 8. In the undisturbed flat-plate region, the most energetic frequency is centered about $f\delta/U_\infty = 2.0$, a characteristic frequency of the energetic scales in the turbulent boundary layer.[10] As the flow approaches the interaction region, the energetic frequency is characterized by a wide range of frequencies, and the most energetic frequency shifts to much lower frequencies between $f\delta/U_\infty = 0.01 - 0.2$, which is associated with the low-frequency shock wave motion. As the flow develops further downstream, the central frequency recovers back to $f\delta/U_\infty = 1$, smaller than that in the undisturbed turbulent boundary layer. This variation trend is in accordance with the existed study.[10,28]

C. Instantaneous flow characteristics

Q-criterion[29] has been widely used to visualize the turbulent coherent structures. The instantaneous iso-surfaces of Q, colored by the instantaneous streamwise vorticity ω_x, are shown in Fig. 9. Given the relatively high threshold of Q-criterion used in the visualizations,
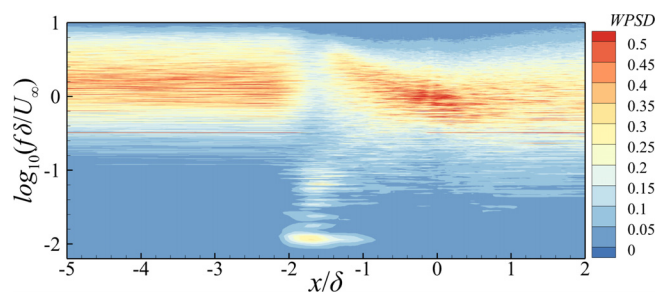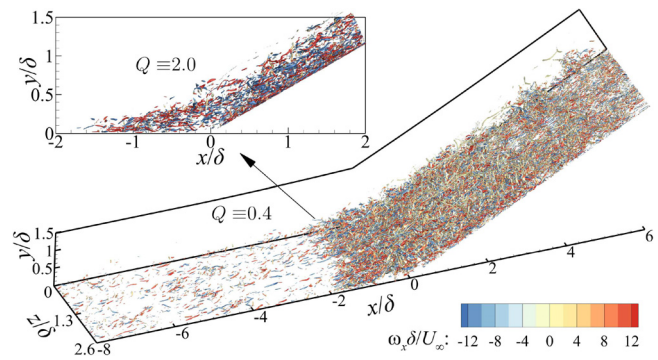

FIG. 9. Instantaneous turbulent coherent structures visualized using the iso-surfaces of Q. The iso-surfaces are colored by the instantaneous streamwise vorticity ω_x.

few vortical structures are visible in the incoming turbulent boundary layer. These vortical structures appear mainly as streamwise vortices, known as the leg of horseshoe-like vortices, and seem randomly distributed in the near wall region.[30] As the flow approaches the interaction region, the vortical structures are significantly increased. In addition to the streamwise-oriented vortices, some spanwise-oriented vortices are formed, behaving like three-dimensional vortices. The enlarged drawing of vortical structures around the compression corner in the side view is presented in the top left part of Fig. 9 with $Q \equiv 2.0$. One can see that the energetic vortical structures are lifted up away from the wall, while few vortical structures exist within the flow separation region around the compression corner [Fig. 7(a)]. In the downstream of the flow reattachment, rich vortical structures are also visible although it appears that the intensity of turbulent structures tends to weaken gradually.

D. Turbulent kinetic energy

The shear layer around the compression corner has been reported to play an important role in the turbulence amplification.[3,5,9] As such, it is necessary to analyze the characteristics of the shear layer before studying the impact of the SWTBLI on the turbulent statistics. The shear layer denoted by the mean spanwise vorticity $\langle\omega_z\rangle = \frac{\partial\langle v\rangle}{\partial x} - \frac{\partial\langle u\rangle}{\partial y}$[5,10] is shown in Fig. 10. One can see that as the flow approaches the interaction zone around $x/\delta = -2.0$, the shear layer does not detach from the wall until

FIG. 8. Contours of the weighted power spectral density $WPSD$ of the wall pressure in the vicinity of the interaction region.
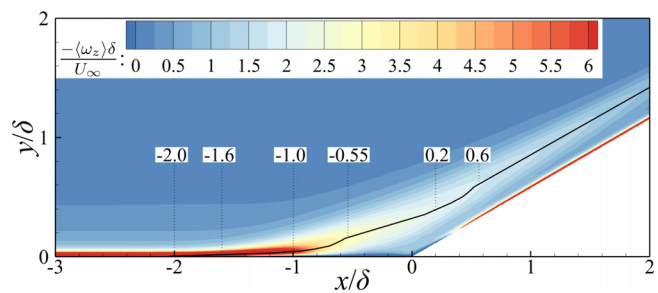

FIG. 10. Contours of the mean spanwise vorticity $-\langle\omega_z\rangle$ in the x–y plane near the compression corner. The solid line denotes the local peak of $-\langle\omega_z\rangle$ along the y direction at each streamwise position.

$x/\delta = -1.6$. It is from $x/\delta = -1.0$ that the shear layer shows an apparent upward deflection with decreased intensity as the flow travels downstream, and its core (represented by solid line, which is composed of the local peak along the y direction at each x) tends to shift away from the wall. With a close examination of the solid line, it is interesting to find that the line consists of two sections with quasi-straight line. The first section starts approximately from $x/\delta = -0.55$ to 0.2 with the inclination angle being about $16.5°$. The second one is located downstream of $x/\delta \approx 0.6$ and is parallel to the ramp wall, and meanwhile, the strong wall shear layer begins to re-develop.

The turbulent kinetic energy (TKE) is defined as $\langle k \rangle = 0.5(\langle u''u'' \rangle + \langle v''v'' \rangle + \langle w''w'' \rangle)$, where $\langle u''u'' \rangle$, $\langle v''v'' \rangle$, and $\langle w''w'' \rangle$ are the Reynolds normal stress components along the x, y, and z directions, respectively. Figure 11 presents the contour of $\langle k \rangle$ in the x–y plane around the compression ramp. In comparison with the incoming boundary layer, it is clear that the intensity of $\langle k \rangle$ has an apparent increase in the interaction region, which is consistent with the existed DNS results.[5,7] There exist two separated maxima of $\langle k \rangle$. The intensity of $\langle k \rangle$ in the upstream maximum point is slightly larger (Fig. 12), and the value is around 4.4 times its peak value in the incoming undisturbed turbulent boundary layer.

At the starting position of the interaction region around $x/\delta = -2.0$, there is no obvious change of $\langle k \rangle$ compared to that at $x/\delta = -3.0$. Downstream of this position, the intensity of $\langle k \rangle$ tends to increase significantly. The peak value of $\langle k \rangle$ at $x/\delta = -1.6$ exceeds 2.0 times that at $x/\delta = -3.0$ (Fig. 12), while the peak location exhibits no distinguishable moving away from the wall (Fig. 11), indicating that the TKE amplification starts before the detachment of the shear layer. Consequently, the free shear layer, at least upstream of $x/\delta = -1.6$, should not be the key factor for the TKE amplification, although the free shear layer has been reported to be the dominant factor for the turbulence amplification in the SWTBLI region.[9,10] Figure 12 shows half of the Reynolds normal stress at the vertical position where $\langle k \rangle$ peaks. One can see that the increment in $\langle k \rangle$ at $x/\delta = -1.6$ is dominated by the streamwise velocity fluctuations $\langle u''u'' \rangle$. It is noteworthy that the unsteady shock wave oscillation occurs in this region (Fig. 8), leading to the oscillation of the separation bubble[10] and hence the streamwise velocity. This flow phenomenon suggests that the increased intensity of $\langle k \rangle$ may be related to the shock wave unsteadiness. As the flow develops further downstream from $x/\delta = -1.6$ to -1.0, the peak position of $\langle k \rangle$
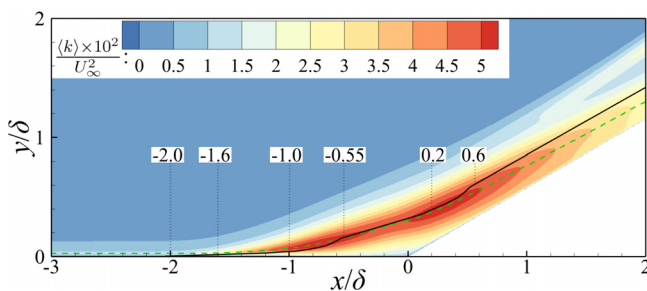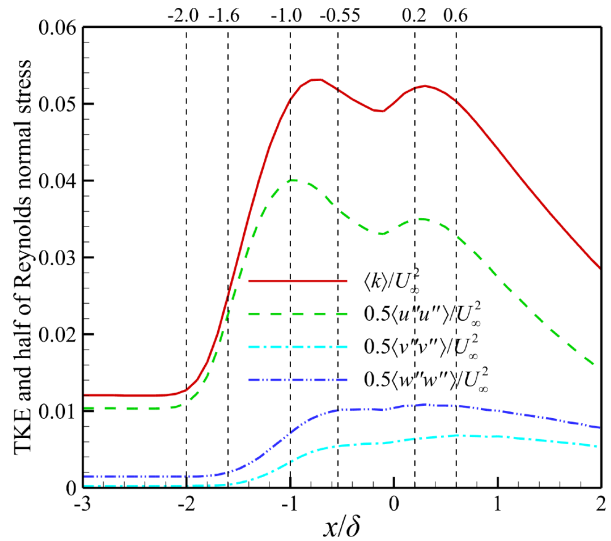

FIG. 12. Streamwise distribution of $\langle k \rangle$ and half of the Reynolds normal stresses at the vertical position where $\langle k \rangle$ peaks.

appears to shift gradually away from the wall (Fig. 11) with increased intensity. Meanwhile, the intensity of $\langle v''v'' \rangle$ and $\langle w''w'' \rangle$ begins to increase gradually, and they play increasingly important contribution on the TKE amplification.

The dashed line in Fig. 11 is the locus of points where $\langle k \rangle$ peaks along the y direction at each point in x. Comparing the solid and dashed lines, one can see that the maximum $\langle k \rangle$ follows the core of the shear layer in the region downstream of $x/\delta = -0.55$. This suggests that the TKE amplification is closely related to the formation of the free shear layer. This is reasonable since, on the one hand, the shear layer itself is an important source of the production of turbulent fluctuations. On the other hand, as the shear layer rolls up away from the wall, abundant vortical structures (see Fig. 9) are produced owing to the Kelvin–Helmholtz instability,[10–12] which further enhances the turbulent fluctuations nearby.

Downstream of $x/\delta = 0.6$ (around the reattachment point), the line for the peak position of $\langle k \rangle$ is parallel to the ramp wall with gradually decreased intensity as the flow travels downstream, similar to that of the separated shear layer. Nevertheless, the intensity of $\langle k \rangle$ remains relatively high. One reason for the turbulence amplification in this region can be attributed to the generation and more importantly the shedding of the turbulent vortical structures in the free shear layer. It is worth emphasizing that the peak position of $\langle k \rangle$ around the shock wave system is not shown, since the turbulence amplification by the shock wave has been well studied using the linear interaction analysis and the linearized Rankine–Hugoniot jump relations,[31,32] and will not be analyzed in the present paper.

In summary, in the interaction region before the detachment of the shear layer, the intensity of the TKE has an apparent increase. As the flow develops downstream, $\langle k \rangle$ remains the high intensity with its peak position following the core of the free shear layer, suggesting that the free shear layer and the resultant Kelvin–Helmholtz instability are the key factor for the TKE amplification.

FIG. 11. Contours of the turbulent kinetic energy $\langle k \rangle$ in the x–y plane. The solid and dashed lines denote the local peak of $-\langle \omega_z \rangle$ and $\langle k \rangle$ along the y direction at each streamwise point.

1. Production term of turbulent kinetic energy

To further explore the underlying mechanism for the significantly increased intensity of $\langle k \rangle$ in the SWTBLI region, the TKE production term, P_k, is analyzed in this section. P_k has been widely studied and can be written as

$$P_k = -\langle u''v'' \rangle \left(\frac{\partial \langle u \rangle}{\partial y} + \frac{\partial \langle v \rangle}{\partial x} \right) \underbrace{}_{P_s} - \underbrace{\langle u''u'' \rangle \frac{\partial \langle u \rangle}{\partial x}}_{P_x} - \underbrace{\langle v''v'' \rangle \frac{\partial \langle v \rangle}{\partial y}}_{P_y}, \quad (5)$$

where the three terms in the right-hand side are the shear production term P_s, streamwise deceleration term P_x, and vertical deceleration term P_y, respectively.

The contour of P_k in the x–y plane around the compression ramp is presented in Fig. 13(a). It is clear that as the flow approaches the interaction region, the intensity of P_k is significantly increased, and the maximum value occurs around the core of the separated shear layer or the shock wave. The three production term components P_s, P_x, and P_y are shown in Figs. 13(b)–13(d). In the incoming boundary layer, P_s, as expected, is the dominant term, while the other two terms play negligible influence. As the flow enters the interaction region in the range between $x/\delta = -2.0$ and -1.0, the intensity of P_x, the streamwise deceleration term, is significantly increased, acting as the dominant term of P_k. This finding is consistent with the DNS results in the supersonic impinging SWTBLIs by Fang et al.[5] who also pointed out that the streamwise deceleration term was an important contributor for the turbulence amplification in the initial stage of the interaction region. From Fig. 7(a), one can see that the streamwise velocity appears to decelerate in this region, leading to negative $\frac{\partial \langle u \rangle}{\partial x}$. Meanwhile, the streamwise velocity fluctuation $\langle u''u'' \rangle$ is increased significantly (Fig. 12). This indicates that the TKE amplification is related to the streamwise deceleration, instead of the separated shear layer. This can well explain why $\langle k \rangle$ has an apparent increase (Fig. 11) before the free shear layer is developed. Nevertheless, the underlying mechanism for the amplification of $\langle u''u'' \rangle$ needs further exploration, which will be studied in Sec. III D 2 using the spectral analysis.

In the interaction region downstream of $x/\delta = -0.55$, P_x is also the dominant term of P_k, as seen in Figs. 13(b)–13(d). In this zone, the direction of both the mean streamlines and separated shear layer has an obvious deflection, and hence, it is not appropriate to continue to regard P_x as the streamwise deceleration function. The shear layer coordinate system has been applied in the interaction region,[11,12] and this layer is found to follow the properties of the canonical mixing layer.[11] In addition, it has been reported that the profiles of the mean velocity and Reynolds stress in the shear layer coordinate system collapse well.[11,12] This indicates that it is physically correct and meaningful to analyze the turbulent characteristics in the shear layer coordinate system. As stated before, there exist two-straight line sections of the separated shear layer in the interaction region (Fig. 10): One is located between $x/\delta = -0.55$ and 0.2; the other is downstream of $x/\delta = 0.6$. In consequence, two shear layer coordinate systems, i.e., (x_a, y_a) and (x_b, y_b), can be defined accordingly, as illustrated in Fig. 14. The longitudinal x_ζ-axis ($\zeta = a, b$) is oriented along the center of the shear layer (x_b is also parallel to the ramp wall), and y_ζ-axis is perpendicular to x_ζ-axis pointing away from the wall. By applying the coordinate transformation, the velocity component in the shear layer
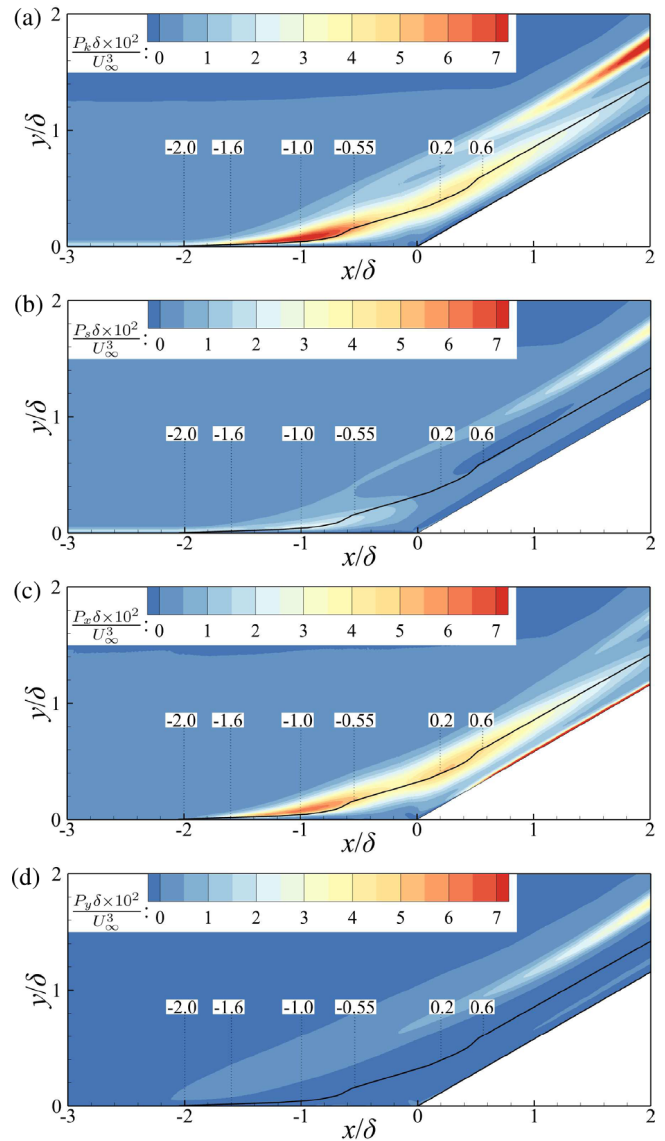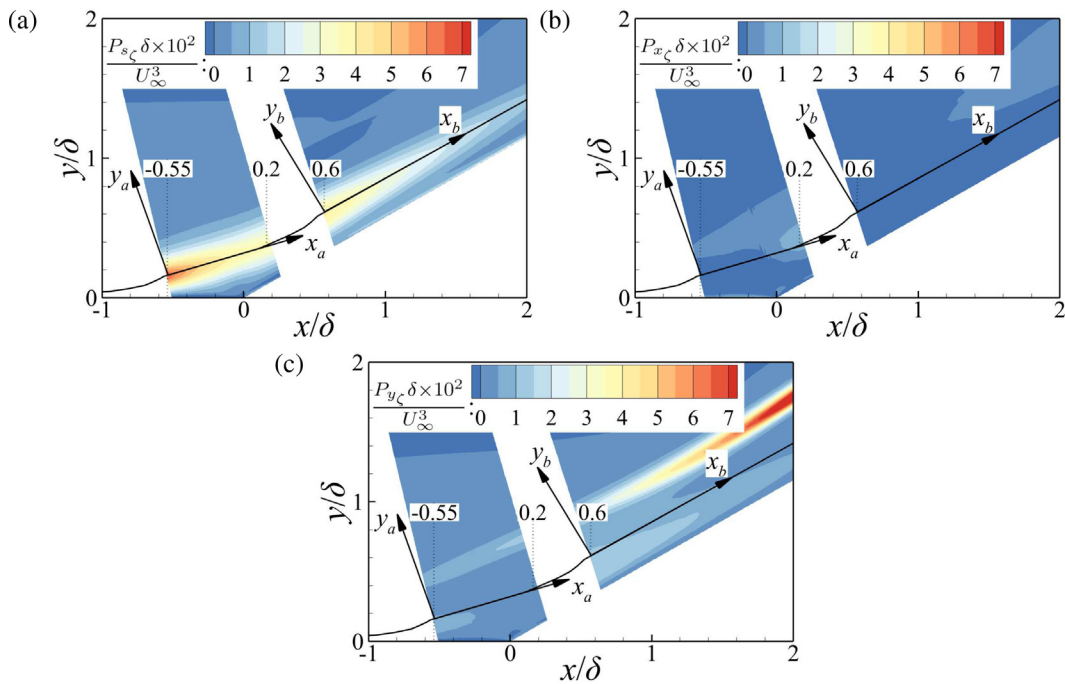

FIG. 13. Contours of (a) the TKE production P_k and its three components; (b) the shear production term P_s; (c) streamwise deceleration term P_x; and (d) vertical deceleration term P_y in the x–y plane around the compression ramp.

coordinate system x_ζ–y_ζ can be calculated. Consequently, the three components of the TKE production term are expressed as

$$p_{s_\zeta} = -\langle u''_\zeta v''_\zeta \rangle \left(\frac{\partial \langle u_\zeta \rangle}{\partial y_\zeta} + \frac{\partial \langle v_\zeta \rangle}{\partial x_\zeta} \right), \quad p_{x_\zeta} = -\langle u''_\zeta u''_\zeta \rangle \frac{\partial \langle u_\zeta \rangle}{\partial x_\zeta},$$

$$p_{y_\zeta} = -\langle v''_\zeta v''_\zeta \rangle \frac{\partial \langle v_\zeta \rangle}{\partial y_\zeta}, \quad \zeta = a, b. \quad (6)$$

Figure 14 shows contours of the production term components defined in the shear layer coordinate system. One can see that the shear production term p_{s_ζ} is the dominant contributor of P_k for the two sub-regions in the shear layer coordinate system. This finding

FIG. 14. Contours of the TKE production components: (a) the shear production term p_{s_ζ}, (b) streamwise deceleration term p_{x_ζ}, and (c) vertical deceleration term p_{y_ζ} in the shear layer coordinate system.

further confirms that the TKE amplification is closely related to the free shear layer. It is also noteworthy that the intensity of p_{s_ζ} tends to decrease once the mixing layer is established. This is because the intensity of $-\langle\omega_z\rangle$ tends to decrease as the flow develops from $x/\delta = -0.55$ (Fig. 10).

In summary, in the interaction region before the detachment of the shear layer, the TKE production is dominated by the streamwise deceleration part instead of the shear driven, originating from the product of $\langle u''u''\rangle$ and $-\frac{\partial\langle u\rangle}{\partial x}$. Once the detached separated shear layer is generated, the shear production term of the TKE acts as the key factor, and energetic turbulent vortical structures are produced, owing to the free shear layer and Kelvin–Helmholtz instability.

2. Spectral analysis of turbulent kinetic energy

For the statistically stationary process, the auto-correlation function of the streamwise velocity fluctuation $\psi(t) = \frac{1}{\sqrt{\bar\rho}}\sqrt{\rho(t)}u''(t)$ with finite variance can be defined as $R_u(\tau) = \overline{\psi(t)\psi(t+\tau)}$ [$R_{uu}(0) = \langle u''u''\rangle$ with this definition]. Let $S_{uu}(\omega)$ (ω is the angular frequency) denotes the Fourier transform of the correlation function $R_{uu}(\tau)$. Then, $R_{uu}(\tau)$ and $S_{uu}(\omega)$ form a Fourier transform pair,[33]

$$S_{uu}(\omega) = \frac{1}{2\pi}\int_{-\infty}^{\infty} R_{uu}(\tau)e^{-i\omega\tau}d\tau = \frac{1}{\pi}\int_{0}^{\infty} R_{uu}(\tau)\cos(\omega\tau)d\tau,$$

$$R_{uu}(\tau) = \int_{-\infty}^{\infty} S_{uu}(\omega)e^{i\omega\tau}d\omega = 2\int_{0}^{\infty} S_{uu}(\omega)\cos(\omega\tau)d\omega. \quad (7)$$

For $\tau = 0$, one can immediately see from Eq. (7) that[33]

$$R_{uu}(0) = \langle u''u''\rangle = 2\int_{0}^{\infty} S_{uu}(\omega)d\omega = \int_{0}^{\infty} 4\pi S_{uu}(2\pi f)df$$
$$= \int_{0}^{\infty} E_{uu}(f)df, \quad (8)$$

where $E_{uu}(f) = 4\pi S_{uu}(2\pi f)$ is the energy spectra density of $\langle u''u''\rangle$, showing how the streamwise kinetic energy is distributed as a function of frequency f. Based on the same operations, $\langle v''v''\rangle$, $\langle w''w''\rangle$, $\overline{p'p'}$, and $\langle k\rangle$ can also be expressed as

$$\langle v''v''\rangle = \int_{0}^{\infty} E_{vv}(f)df \quad \text{at } \psi(t) = \frac{1}{\sqrt{\bar\rho}}\sqrt{\rho(t)}v''(t),$$

$$\langle w''w''\rangle = \int_{0}^{\infty} E_{uu}(f)df \quad \text{at } \psi(t) = \frac{1}{\sqrt{\bar\rho}}\sqrt{\rho(t)}w''(t),$$

$$\overline{p'p'} = \int_{0}^{\infty} E_{pp}(f)df \quad \text{at } \psi(t) = p'(t), \quad (9)$$

$$\langle k\rangle = \int_{0}^{\infty} E_k(f)df \quad \text{at } E_k(f) = \frac{1}{2}(E_{uu}(f) + E_{vv}(f) + E_{ww}(f)).$$

Equations (8) and (9) give a spectral representation of the turbulent fluctuations as the sum of Fourier modes at different frequencies. Figure 15 shows the streamwise evolution of $\langle k\rangle$ and the Reynolds normal stresses at the vertical position where $\langle k\rangle$ peaks. One can see that the results from the spectral analysis are in good accordance with the statistical results from the density-weighted averaging, verifying the accuracy of the spectral analysis. One possible reason for the error between them may result from the different sample numbers. For the density-weighted averaging, the instantaneous flow field is sampled
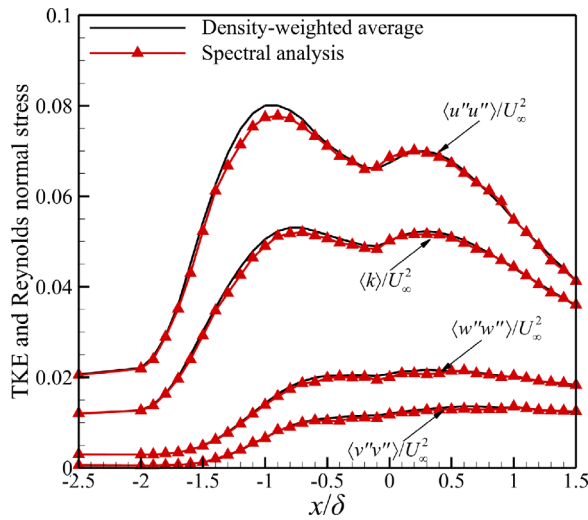
FIG. 15. Streamwise evolution of $\langle k \rangle$ and Reynolds normal stresses at the vertical position where $\langle k \rangle$ peaks.

every 5 time steps, and 250 000 samples of instantaneous flow field are collected, covering a non-dimensional period of 1000 δ/U_∞. In contrast, for the spectral analysis, the instantaneous flow field is sampled every 50 time steps with the same time range.

Figure 16 shows the premultiplied energy spectra of $\langle k \rangle$ at $x/\delta = -2.5$ and $x/\delta = -1.6$ to illustrate the distribution of energy across the dimensionless frequency $f\delta/U_\infty$. In this study, the energy spectra are divided into three sections, namely, the low-frequency range with $f\delta/U_\infty < f_L = 0.1$, the high-frequency range with $f\delta/U_\infty > f_H = 2.0$, and the median-frequency between them. In the undisturbed turbulent boundary layer, the turbulence energy exists mainly in the median-frequency range, while in the low- and high-frequency
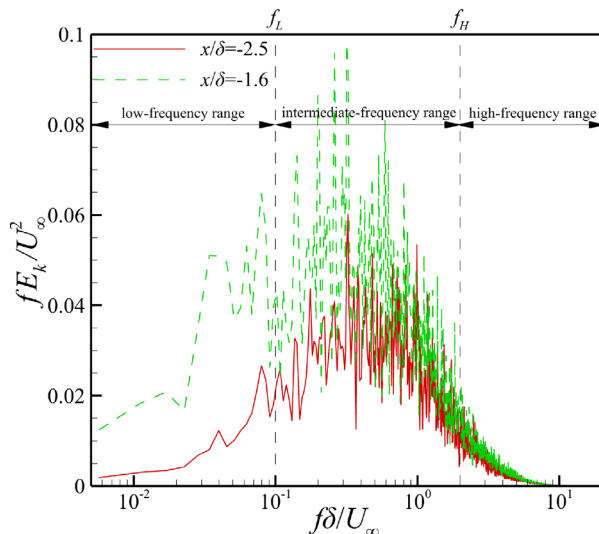

FIG. 16. Premultiplied energy spectra of $\langle k \rangle$ at the vertical position where $\langle k \rangle$ peaks for $x/\delta = -2.5$ and $x/\delta = -1.6$.

ranges, the energy content is much less. In the interaction region at $x/\delta = -1.6$, the turbulence energy has an apparent increase, especially in the low-frequency range. Comparing the low-frequency characteristics of the wall pressure in Fig. 8, it is expected that the low-frequency energy spectra of $\langle k \rangle$ are closely related to the low-frequency unsteadiness of the shock wave.

To quantitatively analyze the energy content in the three frequency ranges, the integrated energy for each range at each streamwise position is introduced as

$$\langle k \rangle_L = \int_0^{f_L} E_k(f) df, \quad \langle k \rangle_M = \int_{f_L}^{f_H} E_k(f) df, \quad \langle k \rangle_H = \int_{f_H}^{\infty} E_k(f) df.$$
(10)

Based on Eq. (10), the turbulent kinetic energy $\langle k \rangle$ is subdivided into three parts. Figure 17(a) shows the streamwise distribution of the three components of $\langle k \rangle$. In the initial stage of the interaction region from $x/\delta = -2.0$ to $x/\delta = -1.6$, the increment in $\langle k \rangle$ mainly results from $\langle k \rangle_L$, and the low-frequency energy proportion ($\langle k \rangle_L / \langle k \rangle$) increases from 21% at $x/\delta = -2.5$ to 43% at $x/\delta = -1.6$ [Fig. 17(b)]. It has been well documented in the literature[10,28] that the low-frequency oscillations occur in the initial stage of the SWTBLI flows, which can also be seen in Fig. 8. Consequently, it is not surprising that the spectral energy in the low-frequency range dominates the increase in $\langle k \rangle$ nearby. To further illustrate this, the streamwise distribution of the proportion of the three parts of $\overline{p'p'}$ is presented in Fig. 17(c). It is clearly seen that the low-frequency proportion has a dramatic increase at $x/\delta = -1.6$, exceeding 50%, while the corresponding proportion at $x/\delta = -2.5$ is only 1.8%.

As the flow develops further downstream, the low-frequency energy $\langle k \rangle_L$ continues to increase until $x/\delta = -1.2$. Meanwhile, the median-frequency energy $\langle k \rangle_M$ tends to increase at a faster speed. Both $\langle k \rangle$ and $\langle k \rangle_M$ reaches a local peak (the upstream maximum) at around $x/\delta = -0.7$. Helm et al.[12] pointed out that the median-frequency content in the interaction region was associated with the mixing layer turbulence. This further confirms the dominant role of the free shear layer and Kelvin–Helmholtz instability on the formation of abundant turbulent vortical structures and the TKE amplification. Apparently, the generation mechanism of the upstream maximum of $\langle k \rangle$ is closely related to the mixing layer turbulence. On the one hand, the separated shear layer has been established at $x/\delta = -0.7$; on the other hand, the intensity of $-\langle \omega_z \rangle$ is very high nearby. The similar upstream maximum was also reported by Helm and Martín[34] in the SWTBLI over a relatively large compression angle. Their results also revealed that for the case with a relatively small compression angle, the upstream maximum of $\langle k \rangle$ did not exist,[34,35] which, according to the present results, can be attributed to the absence of the separated shear layer nearby provided that the SWTBLI is so weak that no mean flow separation is induced.

Across the main region of the separated shear layer from $x/\delta = -0.7$ to $x/\delta = 0.5$, the intensity of $\langle k \rangle_L$ and $\langle k \rangle_H$ remains almost unchanged. In contrast, the intensity of $\langle k \rangle_M$ stays in a high level and dominates the streamwise variation of $\langle k \rangle$, which appears to decrease first and then begins to increase from $x/\delta = -0.2$. There exists another local maximum (the downstream maximum) of $\langle k \rangle$ around $x/\delta = 0.2$, and the component $\langle k \rangle_M$ is the key contributor, as seen in Fig. 17(a). Obviously, one reason for the large turbulence
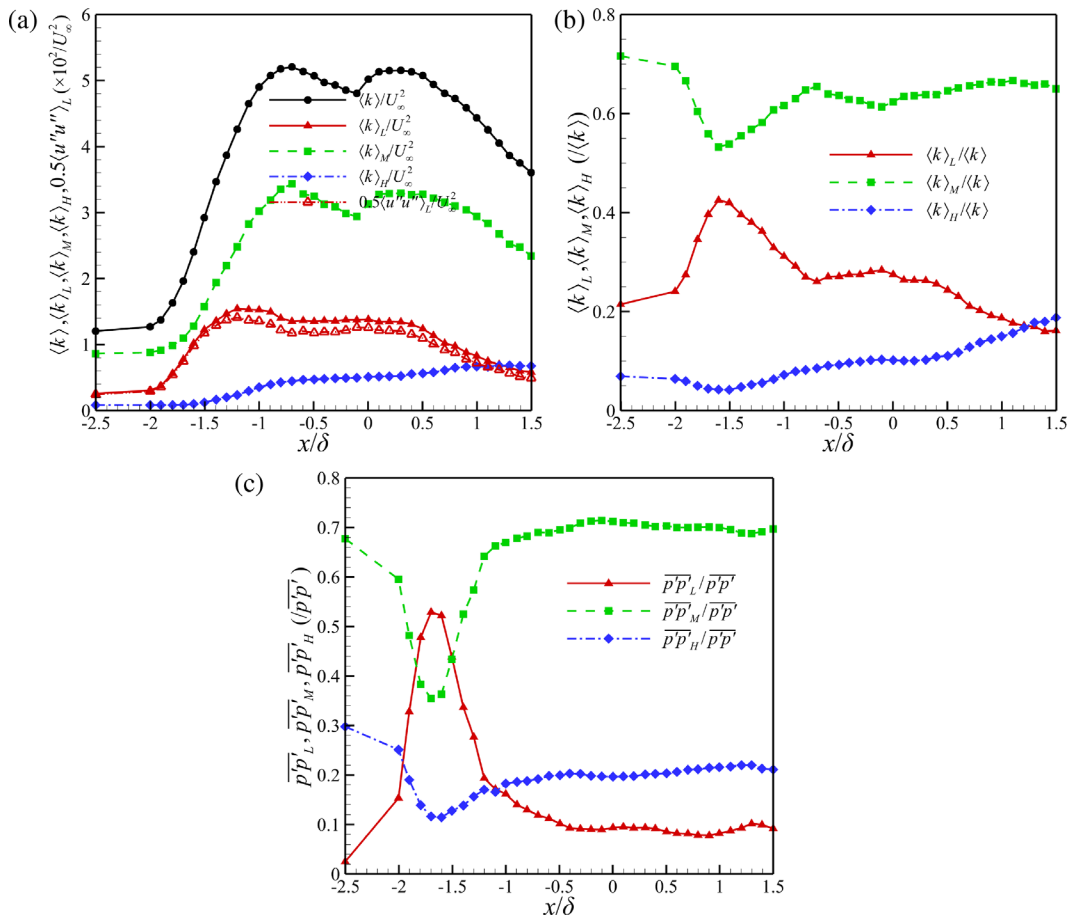
FIG. 17. Streamwise distribution of (a) the three parts of $\langle k \rangle$ with (b) their proportion and (c) the proportion of the three parts of $\overline{p'p'}$.

intensity at $x/\delta = 0.2$ is attributed to the formation of energetic turbulent structures in the separated shear layer and subsequent shedding of these structures into the downstream flow. Nevertheless, this cannot well explain the occurrence of the downstream maximum from the view of mixing layer, since the intensity of $-\langle \omega_z \rangle$ is in the decreased trend nearby (Fig. 10). According to Dolling's study[36] in the SWTBLI over compression ramps, there existed one local maximum of the wall pressure fluctuation (normalized by the local mean value) around the reattachment point, owing to the significant variations of the instantaneous pressure as the separation bubble expanded and contracted.[36] From Fig. 8, it is clear that the most energetic frequency of pressure fluctuations is around $f\delta/U_\infty = 0.5–1.8$, in the range of median-frequency. In consequence, the velocity fluctuations arising from the expansion/contraction of the separation bubble are expected to be in the median-frequency range, leading to the increase in $\langle k \rangle_M$ and ultimately $\langle k \rangle$. Under the combined influence of the mixing layer turbulence and the expansion/contraction of the separation bubble, both $\langle k \rangle_M$ and $\langle k \rangle$ reach a local peak (the downstream maximum) at around $x/\delta = 0.2$.

In summary, the TKE amplification before the detachment of the shear layer is closely related to the low-frequency unsteadiness of the shock wave, which leads to the rapid increase in $\langle u''u'' \rangle$. Once the free shear layer is established, the increment in $\langle k \rangle$ is dominated by the energy content in the median-frequency range, arising from the mixing layer turbulence. There exist two separated TKE maxima: The upstream one is attributed to the mixing layer turbulence; the downstream one is caused by the mixing layer turbulence and the expansion/contraction of the separation bubble.

E. Temperature field

The contours of the spanwise-averaged mean temperature in the $x–y$ plane is shown in Fig. 18(a). One can see that the maximum mean aerodynamic heating is produced in the vicinity of the compression corner where the reverse flow occurs, and the maximum mean temperature is about 6.5 T_∞. It is noteworthy that the amplification of the temperature is much larger than that in the supersonic SWTBLIs,[37,38] even for the very strong SWTBLIs at Mach 3.0[38] that the maximum temperature is about 2.8 T_∞. The temperature fluctuation (TF) normalized by the free-stream temperature is presented in Fig. 18(b). It is clear that an apparent increase in the TF is obtained in the interaction region. The largest intensity of $\overline{T'T'}/T_\infty^2$ in the upstream boundary layer is about 0.7, while the maximum value in the interaction region is up to 2.0, with an amplification factor of 2.9. It is also noteworthy that when $x/\delta > 1.6$, there exists a local peak around the shock wave.
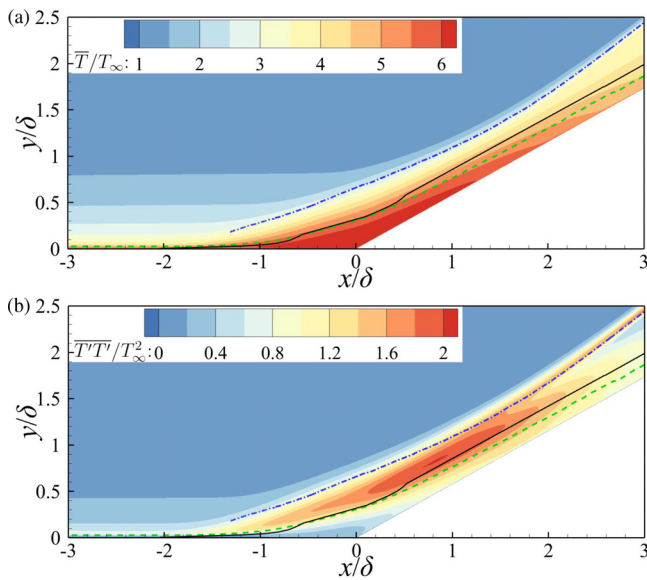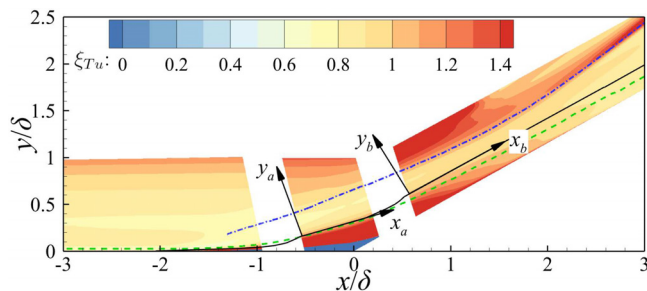
FIG. 18. Contours of the spanwise-averaged (a) mean temperature and (b) $\overline{T'T'}$ normalized by T_∞^2 in the x–y plane. The solid, dashed, and dash-dotted lines denote the local peak of $-\langle\omega_z\rangle$, $\langle k\rangle$, and mean pressure gradient $|\nabla\overline{p}|$ along the y direction at each streamwise point.

In the compressible turbulent boundary layer, the strong Reynolds analogy relationship between the TF and the streamwise velocity fluctuation can be expressed as[14,39]

$$\xi_{Tu} = \frac{\sqrt{\overline{T'T'}}/\overline{T}}{(\gamma-1)\overline{Ma}^2\sqrt{\overline{u'u'}}/\overline{u}} \approx 1. \qquad (11)$$

Figure 19 shows contour of the strong Reynolds analogy relationship ξ_{Tu} in the x–y plane. In the upstream turbulent boundary layer, ξ_{Tu} mainly lies in the range of 0.8 to 1.0, which is consistent with the value from Duan *et al.*[15] at the similar wall-recovery temperature ratio. In the vicinity of the compression corner ($-0.5 < x/\delta < 0.3$), the mean velocity and its fluctuation in Eq. (11) are defined in the shear layer coordinate system $x_a - y_a$. One can see that the value of ξ_{Tu} above the separated shear layer is similar to that in the boundary layer.

FIG. 19. Contours of the strong Reynolds analogy relationship ξ_{Tu} in the x–y plane. The solid, dashed, and dash-dotted lines denote the local peak of $-\langle\omega_z\rangle$, $\langle k\rangle$, and mean pressure gradient $|\nabla\overline{p}|$ along the y direction at each streamwise point.

In the near-wall region below $y/\delta < 0.1$, ξ_{Tu} is negative, which correlates with the negative velocity resulting from the flow separation. Downstream of the separation region ($x/\delta > 0.6$), the value of ξ_{Tu} in the most region is close to 1.0, especially in the region below the shock wave (denoted by the local peak of $|\nabla\overline{p}|$ along the y direction at each streamwise point). In the near wall region around $x/\delta = 0.8$ where the flow reattachment occurs, the value of ξ_{Tu} exceeds 1.4, revealing an apparent increase compared to that in the boundary layer. It is noteworthy that the value of ξ_{Tu} above the shock wave reveals an increase especially in the initial region. One possible reason is that it is not appropriate to use the shear layer coordinate in this region since the main flow direction is actually along the x-axis rather than the x_b-axis, and obviously, the velocity along the x-axis is larger than that along the x_b-axis. Overall, the strong Reynolds analogy relationship ξ_{Tu} behaves well in the interaction region below the shock wave.

1. Spectral analysis of temperature fluctuation in the interaction region

With the same operation applied in Eq. (9), $\overline{T'T'}$ can be expressed as

$$\overline{T'T'} = \int_0^\infty E_{TT}(f)df \quad \text{at } \psi(t) = T'(t). \qquad (12)$$

Figure 20 shows the premultiplied energy spectra of $\overline{T'T'}$ at $x/\delta = -2.5$, $x/\delta = -1.6$, and $x/\delta = 1.0$ to exhibit the energy content across the dimensionless frequency $f\delta/U_\infty$. Consistent with the previous definition used in the TKE, the energy spectra of $\overline{T'T'}$ are also divided into three sections with $f_L = 0.1$ and $f_H = 2.0$. In the undisturbed turbulent boundary layer, the energy content exists mainly in the median-frequency range, while in the low- and high-frequency ranges, the energy content is much less. As the flow enters the interaction region at $x/\delta = -1.6$, it appears that the energy content in the low-frequency range has an apparent increase, while the
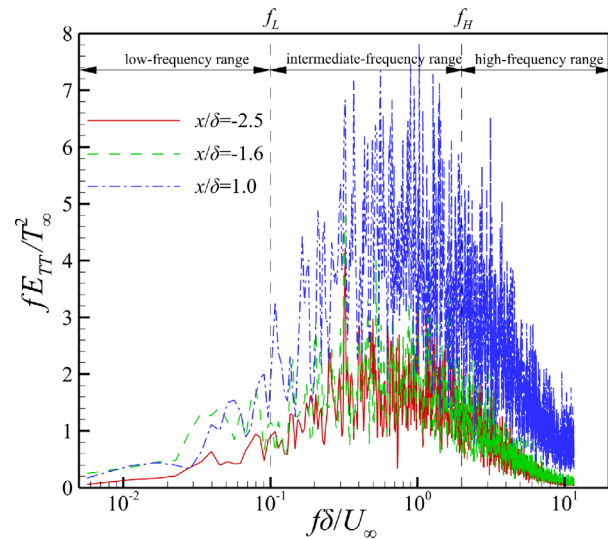
FIG. 20. Premultiplied energy spectra of $\overline{T'T'}$ at the vertical position where $\overline{T'T'}$ peaks for $x/\delta = -2.5$, $x/\delta = -1.6$, and $x/\delta = 1.0$.
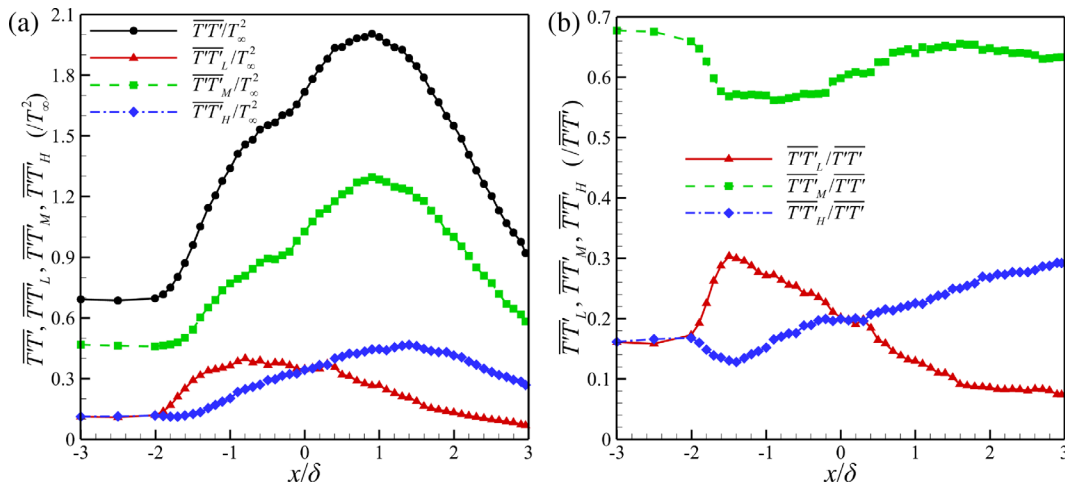
FIG. 21. Streamwise distribution of (a) $\overline{T'T'}$ as well as its three parts and (b) their proportion in the interaction region at the vertical position where $\overline{T'T'}$ peaks.

other two parts show much less variation. This indicates that the low-frequency unsteadiness plays a dominant role in the increase in $\overline{T'T'}$ in the initial stage of the SWTBLI flows, which is in accordance with that of the TKE. The blue dash-dotted line shows the premultiplied energy spectra at $x/\delta = 1.0$ where the intensity of $\overline{T'T'}$ is the largest in the interaction region. It is clear that the energy content in each frequency range is significantly increased compared to that in the boundary layer.

To quantitatively analyze the energy content of $\overline{T'T'}$ in the three frequency ranges, the integrated energy for each range at each streamwise position is performed based on Eq. (10). Figure 21(a) shows the streamwise distribution of $\overline{T'T'}$ and its three parts. In the initial stage of the interaction region from $x/\delta = -2.0$ to $x/\delta = -1.6$, the increment in $\overline{T'T'}$ mainly results from $\overline{T'T'}_L$, and the low-frequency energy proportion ($\overline{T'T'}_L/\overline{T'T'}$) increases from 16% to 32% [Fig. 21(b)]. This variation is quite similar to that of the TKE, both of which are caused by the low-frequency oscillations nearby. As the flow moves further downstream, the low-frequency energy $\overline{T'T'}_L$ continues to increase until $x/\delta = -0.9$, from where it begins to decrease gradually.

Across the interaction region, the median-frequency energy content acts as the main contributor of $\overline{T'T'}$ and dominates its streamwise variation. Both $\overline{T'T'}$ and $\overline{T'T'}_M$ achieve the largest intensity at $x/\delta = 1.0$. Similar to the TKE, it is expected that the amplification of $\overline{T'T'}_M$ is closely related to the energetic turbulent structures in the separated shear layer and subsequent shedding of these structures into the downstream flow. The intensity of $\overline{T'T'}_H$ appears to increase first and then tends to decrease, peaking at $x/\delta = 1.4$. Another noteworthy phenomenon is that the proportion of $\overline{T'T'}_H$ has an apparent increase, from 13% at $x/\delta = 1.4$ to 30% at $x/\delta = 3.0$. In contrast, the proportion of $\overline{T'T'}_L$ is only 7.4%, while the corresponding value in the undisturbed boundary layer is 16%.

2. Spectral analysis of temperature fluctuation around the shock wave

From Fig. 18(b), one can see that there exists a local peak of $\overline{T'T'}$ around the shock wave when $x/\delta > 1.6$. In this section, the energy spectra of $\overline{T'T'}$ around the shock wave where $\overline{T'T'}$ peaks are analyzed.

Figure 22 shows the premultiplied energy spectra of $\overline{T'T'}$ at $x/\delta = 1.6$, $x/\delta = 3.0$, and $x/\delta = 4.0$. The result for $x/\delta = -2.5$ at the vertical position where $\overline{T'T'}$ peaks is also included for comparison. One can see that the energy spectra at $x/\delta = 1.6$ are similar to that in the core interaction region with increased energy content in each frequency range. As the flow moves downstream along the shock wave, the energy content in the low-frequency tends to increase, while $\overline{T'T'}_H$ tends to decrease gradually.

The quantitative comparison of the energy content of $\overline{T'T'}$ in the three frequency ranges is shown in Fig. 23. As the flow moves downstream along the shock wave, the influence of the wall-bounded turbulent flow and the SWTBLIs tends to weaken. Considering that the high-frequency content $\overline{T'T'}_H$ arising from turbulent fluctuations, it is
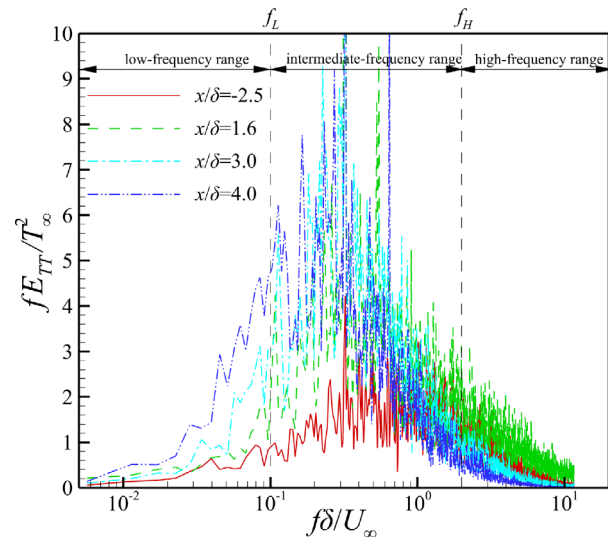

FIG. 22. Premultiplied energy spectra of $\overline{T'T'}$ at the vertical position where $\overline{T'T'}$ peaks around shock wave for $x/\delta = 1.6$, $x/\delta = 3.0$, and $x/\delta = 4.0$. The result at $x/\delta = -2.5$ where $\overline{T'T'}$ peaks is also included for comparison.
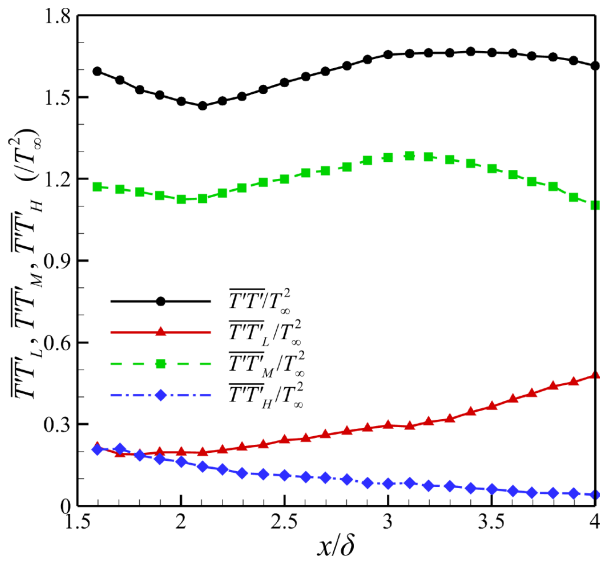
FIG. 23. Streamwise distribution of $\overline{T'T'}$ and its three parts at the vertical position where $\overline{T'T'}$ peaks around the shock wave.

reasonable that the intensity of $\overline{T'T'}_H$ shows a decreasing trend. Meanwhile, the low-frequency range $\overline{T'T'}_L$ tends to increase gradually, owing to the increased intensity of the shock wave [see Fig. 7(b)]. This finding indicates that the low-frequency unsteadiness of the shock wave occurs not only in the initial stage of the interaction region but also around the shock wave. According to the above analysis, there exist two factors that can influence the intensity of $\overline{T'T'}$, i.e., the distance away from the interaction region and the shock wave intensity. Obviously, the first factor can influence the intensity of $\overline{T'T'}_M$. With a closer examination of the contour value in Fig. 8, one can see that there exist median-frequency fluctuations of the wall pressure, implying that the median-frequency motion of the shock wave exists. Consequently, the shock wave intensity can also have an effect on $\overline{T'T'}_M$. Under the combined influence of these two factors, the variation trend of $\overline{T'T'}_M$ behaves more complex, although the variation amplitude appears to be small. From $x/\delta = 1.6$ to $x/\delta = 2.1$, $\overline{T'T'}_M$ appears to weaken slightly, indicating that the influence of the reduced SWTBLI intensity could be larger than that of the increased shock wave intensity. Then, it tends to increase until $x/\delta = 3.1$, due to the increased shock wave intensity. After this, $\overline{T'T'}_M$ begins to decrease again.

IV. CONCLUSION

In this paper, DNSs of a hypersonic turbulent boundary layer over a 30° compression ramp are performed at Mach 6.0 flow with the Reynolds number of $Re_\theta = 6620$. The turbulent kinetic energy (TKE) and temperature fluctuation (TF) amplification mechanism are explored via the TKE production term and the frequency spectrum analysis. The accuracy of the simulation results is validated by comparing the mean velocity profile and turbulence intensity with the existing simulation data. In addition, the grid- and domain-sensitivity study is conducted to ensure that the mesh resolution and the spanwise domain extent are sufficient for the field analysis.

As the flow enters the interaction region, the mean streamwise velocity and temperature tend to decrease and increase, respectively, and a separation bubble occurs around the compression corner with its streamwise length being 1.82δ. The shear layer rolls up and abundant turbulent vortical structures are generated as a result of the Kelvin–Helmholtz instability. Around the separation point in the interaction region, the shock wave presents apparent broadband low-frequency motions in the range of $f\delta/U_\infty = 0.01$–0.2.

In the initial part of the interaction before the detachment of the shear layer, the intensity of the TKE is significantly increased, and its peak position exhibits no distinguishable moving away from the wall. The results show that the TKE amplification is mainly owing to the rapid increase in the streamwise velocity fluctuations. Based on the frequency spectrum analysis, it is found that the TKE and TF amplification is closely related to the low-frequency unsteadiness of the shock wave.

Once the free shear layer is established, the shear component of the TKE production term defined in the shear layer coordinate appears to act as the key contributor for the TKE amplification. This is consistent with the result from the spectrum analysis that the TKE and TF amplifications and their streamwise evolution are dominated by the spectral energy in the median-frequency range, which is mainly caused by the mixing layer turbulence.

The shock wave and interaction intensity play an important role in the TF around the shock wave. As the flow moves downstream along the shock wave, the influence of the SWTBLIs tends to weaken, leading to the decrease in the high-frequency spectral energy content of TF. In comparison, the low-frequency spectral energy tends to increase gradually because of the increased shock wave intensity, implying that the shock wave low-frequency unsteadiness exists not only in the initial stage of the interaction region but also around the main shock wave. Under the combined influence of the shock wave and interaction intensity, the variation trend of median-frequency content appears to weaken first and then tends to increase before decreasing again. The variation amplitude appears to be small and generally dominates the distribution of the TF intensity.

AUTHOR DECLARATIONS
Conflict of Interest

The authors have no conflicts to disclose.

Author Contributions

Tongbiao Guo: Conceptualization (equal); Formal analysis (equal); Writing – original draft (equal). **Ji Zhang:** Methodology (equal);

Software (equal). **Fulin Tong:** Methodology (equal); Validation (equal). **Xinliang Li:** Methodology (equal); Software (equal); Validation (equal).

DATA AVAILABILITY

The data that support the findings of this study are available from the corresponding author upon reasonable request.

REFERENCES

[1] D. S. Dolling, "Fifty years of shock-wave/boundary-layer interaction research: What next?," AIAA J. **39**, 1517–1531 (2001).

[2] A. J. Smits and K.-C. Muck, "Experimental study of three shock wave/turbulent boundary layer interactions," J. Fluid Mech. **182**, 291–314 (1987).

[3] P. Dupont, S. Piponniau, A. Sidorenko, and J. F. Debiève, "Investigation by particle image velocimetry measurements of oblique shock reflection with separation," AIAA J. **46**, 1365–1370 (2008).

[4] M. A. Mustafa, N. J. Parziale, M. S. Smith, and E. C. Marineau, "Amplification and structure of streamwise-velocity fluctuations in compression-corner shock-wave/turbulent boundary-layer interactions," J. Fluid Mech. **863**, 1091–1122 (2019).

[5] J. Fang, A. A. Zheltovodov, Y. Yao, C. Moulinec, and D. R. Emerson, "On the turbulence amplification in shock-wave/turbulent boundary layer interaction," J. Fluid Mech. **897**, A32 (2020).

[6] M. S. Selig, J. Andreopoulos, K. C. Muck, J. P. Dussauge, and A. J. Smits, "Turbulence structure in a shock wave/turbulent boundary-layer interaction," AIAA J. **27**, 862–869 (1989).

[7] M. Wu and M. P. Martin, "Direct numerical simulation of supersonic turbulent boundary layer over a compression ramp," AIAA J. **45**, 879–889 (2007).

[8] S. Priebe, M. Wu, and M. P. Martín, "Direct numerical simulation of a reflected-shock-wave/turbulent-boundary-layer interaction," AIAA J. **47**, 1173–1185 (2009).

[9] S. Pirozzoli and F. Grasso, "Direct numerical simulation of impinging shock wave/turbulent boundary layer interaction at M=2.25," Phys. Fluids **18**, 065113 (2006).

[10] S. Priebe and M. P. Martín, "Low-frequency unsteadiness in shock wave–turbulent boundary layer interaction," J. Fluid Mech. **699**, 1–49 (2012).

[11] P. Dupont, S. Piponniau, and J. P. Dussauge, "Compressible mixing layer in shock-induced separation," J. Fluid Mech. **863**, 620–643 (2019).

[12] C. M. Helm, M. P. Martín, and O. J. Williams, "Characterization of the shear layer in separated shock/turbulent boundary layer interactions," J. Fluid Mech. **912**, A7 (2021).

[13] M. Yu, M. Zhao, Z. Tang, X. Yuan, and C. Xu, "A spectral inspection for turbulence amplification in oblique shock wave/turbulent boundary layer interaction," J. Fluid Mech. **951**, A2 (2022).

[14] M. V. Morkovin, "Effects of compressibility on turbulent flows," Méc. Turbul. **367**, 26 (1962).

[15] L. Duan, I. Beekman, and M. P. Martín, "Direct numerical simulation of hypersonic turbulent boundary layers. Part 2. Effect of wall temperature," J. Fluid Mech. **655**, 419–445 (2010).

[16] G. Gerolymos and I. Vallet, "Pressure, density, temperature and entropy fluctuations in compressible turbulent plane channel flow," J. Fluid Mech. **757**, 701–746 (2014).

[17] B. McManamen, D. Donzis, S. North, and R. Bowersox, "Velocity and temperature fluctuations in a high-speed shock–turbulence interaction," J. Fluid Mech. **913**, A10 (2021).

[18] F. Tong, D. Sun, and X. Li, "Direct numerical simulation of impinging shock wave and turbulent boundary layer interaction over a wavy-wall," Chin. J. Aeronaut. **34**, 350–363 (2021).

[19] T. Guo, J. Fang, J. Zhang, and X. Li, "Investigation of the secondary flow by convergent–divergent riblets in a supersonic turbulent boundary layer over a compression ramp," Phys. Fluids **34**, 106112 (2022).

[20] J. Duan, X. Li, X. Li, and H. Liu, "Direct numerical simulation of a supersonic turbulent boundary layer over a compression–decompression corner," Phys. Fluids **33**, 065111 (2021).

[21] G. Dang, S. Liu, T. Guo, J. Duan, and X. Li, "Direct numerical simulation of compressible turbulence accelerated by graphics processing unit: An open-source high accuracy accelerated computational fluid dynamic software," Phys. Fluids **34**, 126106 (2022).

[22] T. Guo, J. Fang, J. Zhang, and X. Li, "Direct numerical simulation of shock-wave/boundary layer interaction controlled with convergent–divergent riblets," Phys. Fluids **34**, 086101 (2022).

[23] A. Jameson, W. Schmidt, and E. Turkel, "Numerical solution of the Euler equations by finite volume methods using Runge Kutta time stepping schemes," in *14th Fluid and Plasma Dynamics Conference* (AIAA, 1981).

[24] S. Pirozzoli, F. Grasso, and T. B. Gatski, "Direct numerical simulation and analysis of a spatially evolving supersonic turbulent boundary layer at M=2.25," Phys. Fluids **16**, 530–545 (2004).

[25] S. Pirozzoli, F. Grasso, and A. D'Andrea, "Interaction of a shock wave with two counter-rotating vortices: Shock dynamics and sound production," Phys. Fluids **13**, 3460–3481 (2001).

[26] C. Zhang, L. Duan, and M. M. Choudhari, "Direct numerical simulation database for supersonic and hypersonic turbulent boundary layers," AIAA J. **56**, 4297–4311 (2018).

[27] X. Wu and P. Moin, "Direct numerical simulation of turbulence in a nominally zero-pressure-gradient flat-plate boundary layer," J. Fluid Mech. **630**, 5–41 (2009).

[28] M. Grilli, P. J. Schmid, S. Hickel, and N. A. Adams, "Analysis of unsteady behaviour in shockwave turbulent boundary layer interaction," J. Fluid Mech. **700**, 16–28 (2012).

[29] J. Jeong and F. Hussain, "On the identification of a vortex," J. Fluid Mech. **285**, 69–94 (1995).

[30] R. A. Humble, F. Scarano, and B. W. Van Oudheusden, "Unsteady aspects of an incident shock wave/turbulent boundary layer interaction," J. Fluid Mech. **635**, 47–74 (2009).

[31] S. Barre, D. Alem, and J. P. Bonnet, "Experimental study of a normal shock/homogeneous turbulence interaction," AIAA J. **34**, 968–974 (1996).

[32] K. Mahesh, S. K. Lele, and P. Moin, "The influence of entropy fluctuations on the interaction of turbulence with a shock wave," J. Fluid Mech. **334**, 353–379 (1997).

[33] S. B. Pope, *Turbulent Flows* (Cambridge University Press, 2000).

[34] C. M. Helm and M. P. Martín, "Large eddy simulation of two separated hypersonic shock/turbulent boundary layer interactions," Phys. Rev. Fluids **7**, 074601 (2022).

[35] S. Priebe and M. P. Martín, "Turbulence in a hypersonic compression ramp flow," Phys. Rev. Fluids **6**, 034601 (2021).

[36] D. Dolling, "Fluctuating loads in shock wave/turbulent boundary layer interaction: Tutorial and update," in *31st Aerospace Sciences Meeting* (AIAA, 1993).

[37] F. Tong, J. Lai, J. Duan, S. Dong, X. Yuan, and X. Li, "Effect of interaction strength on recovery downstream of incident shock interactions," Phys. Fluids **34**, 125127 (2022).

[38] V. Pasquariello, S. Hickel, and N. A. Adams, "Unsteady effects of strong shock-wave/boundary-layer interaction at high Reynolds number," J. Fluid Mech. **823**, 617–657 (2017).

[39] Y.-S. Zhang, W.-T. Bi, F. Hussain, and Z.-S. She, "A generalized Reynolds analogy for compressible wall-bounded turbulent flows," J. Fluid Mech. **739**, 392–420 (2014).

08 April 2024 03:00:07